REPORT DOCUMENTATION PAGE

AFRL-SR-BL-TR-01-

0203

1. AGENCY USE ONLY (Leave blank)	2. REPORT DATE	3. REPORT TYPE AND DATES COVERED
	2/26/01	Final report 1/1/97 - 9/30/00

4. TITLE AND SUBTITLE

(U) Numerical Study of Leading-Edge Heat Transfer Under Free-Stream Turbulence

5. FUNDING NUMBERS

PE - 61102F
PR - 2307
SA - BS
G - F49620-97-1-0047

6. AUTHOR(S)

Sanjiva K. Lele and Zhongmin Xiong

7. PERFORMING ORGANIZATION NAME(S) AND ADDRESS(ES)

Department of Aeronautics and Astronautics
Stanford University
Stanford, CA 94305-4035

8. PERFORMING ORGANIZATION REPORT NUMBER

9. SPONSORING/MONITORING AGENCY NAME(S) AND ADDRESS(ES)

AFOSR
801 N. Randolph St.
Arlington, VA 22203-1977

10. SPONSORING/MONITORING AGENCY REPORT NUMBER

11. SUPPLEMENTARY NOTES

12a. DISTRIBUTION/AVAILABILITY STATEMENT

Approved for public release; distribution is unlimited

13. ABSTRACT (Maximum 200 words)

The effect of incoming organized disturbance and free-stream turbulence on leading-edge heat transfer is investigated numerically. An optimum length scale is found to give the maximum heat transfer enhancement for the organized disturbance case. Beyond this optimum value, the enhancement decreases with the increase of length scale. For the free-steam turbulence case, large eddy simulation with dynamic SGS model is performed at Reynolds number $Re_D = 10^4$ based on upstream velocity u_∞ and the leading edge diameter of curvature D. The free-stream turbulence is specified as homogeneous, isotropic turbulence with intensity $u'_{rms}/u_\infty = 0.08$ and integral length scale $L/D = 0.4$. Three different regions characterize the interaction of turbulence impinging on the leading edge. For the conditions of the simulations a turbulent heat transfer enhancement of 11% is obtained, which is in fair agreement with the experimental data. The level of heat transfer enhancement is modest because of the Reynolds number is low. However, our results show that in the region very close to the leading edge, the energetic turbulence length scale decreases to the order of 2-3 times the local boundary layer thickness, so a high grid resolution is needed for accurate prediction of heat transfer using large eddy simulation. This is a challenge for future investigations where simulations at higher Reynolds numbers and transonic flow conditions are planned.

Our results motivate a hybrid simulation strategy where the turbulence outside and away from a blade surface is captured using LES techniques while a finer DNS-like grid is embedded within the near-wall region to resolve the smaller eddies responsible for near-wall effects. Such a methodology is being developed in an extension of the work supported under this grant.

14. SUBJECT TERMS	15. NUMBER OF PAGES
Leading-edge heat transfer, turbine heat transfer, free-stream turbulence, large-eddy simulation, stagnation point heat transfer	19
	16. PRICE CODE

17. SECURITY CLASSIFICATION OF REPORT	18. SECURITY CLASSIFICATION OF THIS PAGE	19. SECURITY CLASSIFICATION OF ABSTRACT	20. LIMITATION OF ABSTRACT
Unclassified	Unclassified	Unclassified	UL

NUMERICAL STUDY OF LEADING-EDGE HEAT TRANSFER UNDER FREE-STREAM TURBULENCE

Sanjiva K. Lele, Principal Investigator †
Zhongmin Xiong, Graduate Research Assistant

Department of Mechanical Engineering
Stanford University, Stanford, California 94305

Work supported under grant F49620-97-1-0047 from Air Force Office of Scientific Research

Abstract

The effect of incoming organized disturbance and free-stream turbulence on leading-edge heat transfer is investigated numerically. An optimum length scale is found to give the maximum heat transfer enhancement for the organized disturbance case. Beyond this optimum value, the enhancement decreases with the increase of length scale. For the free-steam turbulence case, large eddy simulation with dynamic SGS model is performed at Reynolds number $Re_D = 10^4$ based on upstream velocity u_∞ and the leading edge diameter of curvature D. The free-stream turbulence is specified as homogeneous, isotropic turbulence with intensity $u'_{rms}/u_\infty = 0.08$ and integral length scale $L/D = 0.1$. Three different regions characterize the interaction of turbulence impinging on the leading edge. For the conditions of the simulations a turbulent heat transfer enhancement of 11% is obtained, which is in fair agreement with the experimental data. The level of heat transfer enhancement is modest because of the Reynolds number is low. However, our results show that in the region very close to the leading edge, the energetic turbulence length scale decreases to the order of 2-3 times the local boundary layer thickness, so a high grid resolution is needed for accurate prediction of heat transfer using large eddy simulation. This is a challenge for future investigations where simulations at higher Reynolds numbers and transonic flow conditions are planned.

Our results motivate a hybrid simulation strategy where the turbulence outside and away from a blade surface is captured using LES techniques while a finer DNS-like grid is embedded within the near-wall region to resolve the smaller eddies responsible for near-wall effects. Such a methodology is being developed in an extension of the work supported under this grant.

1 Introduction

The effect of significant free-stream turbulence generated by the combustor and the upstream blade rows on turbine blade heat transfer is a critical problem in advanced gas turbine design. An improved understanding and accurate prediction of the heat transfer under free-stream turbulence is of essential importance for achieving high turbine inlet temperatures and better thermal efficiency. It is known that free-stream turbulence can cause a large increase in leading edge heat transfer. Many experiments have been conducted to investigate the correlation of the heat transfer enhancement to various flow parameters, such as Reynolds number, Mach number, turbulence intensity, turbulence length scale and the leading edge geometry [1-5]. Ames *et al.* [4] found that both turbulence intensity and turbulence length scale are important in correlating stagnation region heat transfer. Van Fossen *et al.* [5] found the heat transfer augmentation increases with decreasing length scale and the spanwise averaged heat transfer coefficient can be more than 50 percent

† Also affiliated with Department of Aeronautics and Astronautics, Stanford University.

higher than the two-dimensional laminar value. To understand the sensitivity of the heat transfer in the stagnation-region boundary layer to free-stream disturbance, Sutera[6] proposed a theoretical model to study the vorticity amplification due to the stretching of the vortices in the diverging stagnation-flow. Rigby *et al.* [7] numerically simulated spanwise variations in the laminar free-stream in the flow over circular and elliptical leading edges and found the wall heat transfer rate increased by as much as 25 percent. Bae *et al.*[8] performed a numerical simulation of laminar plane stagnation-region flow with organized free-stream spanwise disturbances, and found three different regimes for the amplification/damping of streamwise vortices depending on the disturbance length scale.

Numerical simulations using organized laminar disturbances can isolate various factors such as flow disturbance intensity and length scale that affect leading edge heat transfer, and provide a simple but approximate analogy to the unsteady interacting process between free-stream turbulence and the leading edge. However, the direct computation of free-stream turbulence interacting with the leading edge is very important for understanding the global mechanism of turbulent heat transfer enhancement, and for further developing physically-based turbulence models capable of accounting for the effects of free-stream turbulence. In the present study, we perform a large eddy simulation (LES) of free-stream turbulence interacting with the elliptical leading edge of a finite thickness isothermal flat plate. The flow configuration is based on the experiments previously studied by Van Fossen*et al.*[5]. The purpose is to explore in detail the unsteady interaction process between free-stream turbulence and leading-edge flow and obtain a better understanding of the heat transfer augmentation mechanism. In addition, the simulation also serves as an evaluation of the feasibility of using LES as a tool for accurate heat transfer prediction in the gas turbine environment.

The report is organized as follows. The governing equations and methodology for large eddy simulation are described first, followed by the numerical schemes for the implicit time marching and high order spatial differencing. The generation of free stream turbulence with specified intensity and length scale is discussed together with the inflow boundary conditions for specifying the free-stream turbulence. Both the results from laminar organized disturbances and free-stream turbulence are presented and discussed. The heat transfer enhancement results are compared with reported experimental values, and the typical flow structures at the leading edge are investigated. Concluding remarks summarize the results and discuss future plans for this research.

2 Governing Equations

The governing equations for large eddy simulation are the Favre-filtered compressible continuity and Navier-Stokes equations, written in the non-dimensional primitive variables:

$$\overline{\rho}_{,t} + (\overline{\rho}\tilde{u}_i)_{,i} = 0 \tag{1}$$

$$\overline{\rho}\tilde{u}_{i,t} + \overline{\rho}\tilde{u}_j\tilde{u}_{i,j} = -\overline{p}_{,i} + \frac{1}{Re}[(\tilde{\lambda}\tilde{u}_{j,j})_{,i} + (2\tilde{\mu}\tilde{S}_{ij})_{,j}] - \tau_{ij,j} \tag{2}$$

$$\begin{aligned}\overline{\rho}\tilde{T}_{,t} \quad + \quad & \overline{\rho}\tilde{u}_i\tilde{T}_{,i} + (\gamma-1)\overline{\rho}\tilde{T}\tilde{u}_{j,j} = \frac{\gamma}{PrRe}[\tilde{\kappa}\tilde{T}_{,i}]_{,i} + \\ & \frac{\gamma(\gamma-1)M^2}{Re}[\tilde{\lambda}\tilde{S}_{ii}\tilde{S}_{jj} + 2\tilde{\mu}\tilde{S}_{ij}\tilde{S}_{ij}] - q_{i,i}\end{aligned} \tag{3}$$

with the filtered equation of state for ideal gas

$$\overline{p} = \frac{\overline{\rho}\tilde{T}}{\gamma M^2} \tag{4}$$

In the above equations, ρ is the density, u_i is the velocity vector, p is thermodynamic pressure. M, Re and Pr are the Mach number, Reynolds number, and Prandtl number defined as

$$M = \frac{u_\infty}{c_\infty},\ Re = \frac{\rho_\infty u_\infty D}{\mu_\infty},\ Pr = \frac{\mu_\infty c_p}{\kappa_\infty} \tag{5}$$

Subscript ∞ denotes the far upstream ambient conditions. c is the speed of sound. D is the leading edge diameter of curvature, μ and λ are the first and second coefficients of viscosity, and κ is the thermal

conductivity. $S_{ij} = \frac{1}{2}(u_{i,j} + u_{j,i})$ is the rate-of-strain tensor. Subscripts following a comma denote partial differentiation with respect to the subscript, and the Einstein summation convention is used. The filtered or large scale flow quantity f, denoted by an overbar is given by:

$$\overline{f} = \int_D G(x - x')f(x')dx' \tag{6}$$

where G is some spatial filter-kernel and the integral is over the flow domain. The Favre-averaged quantity, denoted by a tilde is defined as

$$\tilde{f} = \overline{\rho f} \,/\, \overline{\rho} \tag{7}$$

The effect of the small scales are present in the above equation through the sub-grid scale (SGS) stress tensor τ_{ij} in the momentum equation,

$$\tau_{ij} = \overline{\rho}(\widetilde{u_i u_j} - \tilde{u}_i \tilde{u}_j) \tag{8}$$

and the SGS heat flux in the energy equation,

$$q_i = \overline{\rho}(\widetilde{u_i T} - \tilde{u}_i \tilde{T}) \tag{9}$$

Several other subgrid-scale terms have been neglected from the energy equation following the same argument as in [9]. The power law for the molecular viscosity coefficient $\tilde{\mu}$ is employed

$$\tilde{\mu} = \tilde{T}^{0.7} \tag{10}$$

and Stokes' hypothesis is used for the second viscosity coefficient $\tilde{\lambda}$.

3 Dynamic SGS model

To close the momentum and energy equation, τ_{ij} and q_i must be modeled. For τ_{ij}, the trace-free Smagorinsky eddy viscosity model is used

$$\tau_{ij} = \frac{1}{3}q^2\delta_{ij} - 2C\overline{\rho}\Delta^2|\tilde{S}|(\tilde{S}_{ij} - \frac{1}{3}\tilde{S}_{kk}\delta_{ij}) \tag{11}$$

where $q^2 = \tau_{ii}$ is the isotropic part of the SGS Reynolds stress tensor, $\tilde{S}_{ij} = \frac{1}{2}(\tilde{u}_{i,j} + \tilde{u}_{j,i})$ and $|\tilde{S}| = (2\tilde{S}_{ij}\tilde{S}_{ij})^{1/2}$. The SGS energy q^2 is parameterized using Yoshizawa's expression:

$$q^2 = 2C_I\overline{\rho}\Delta^2|\tilde{S}|^2 \tag{12}$$

For the q_i, the eddy diffusivity model is used

$$q_i = -\frac{C\overline{\rho}\Delta^2|\tilde{S}|}{Pr_t}\tilde{T}_{,i} \tag{13}$$

where Pr_t is the SGS turbulent Prandtl number and C is the same as in (11). We use the dynamic procedure to compute the eddy coefficients C, C_I and SGS turbulent Prandtl number Pr_t, which are all functions of instantaneous flow variables. The key concept of the dynamic model is the effective utilization of the large-scale field which is computed directly. This information is brought to bear by introducing a "test filter" with a larger filter width than the resolved grid filter, which generates a second field with scales larger than than the resolved field. Details of the derivation may be found in [9]. Let a spatially test-filtered quantity be denoted by a caret and the width of the test filter is denoted by $\hat{\Delta}$, the SGS coefficients C_I, C can be computed as

$$C_I = \frac{< \mathcal{L}_{kk} >}{< 2(\hat{\overline{\rho}}\hat{\Delta}^2|\hat{\tilde{S}}|^2 - \Delta^2\widehat{\overline{\rho}|\tilde{S}|^2}) >} \tag{14}$$

$$C = \frac{< (\mathcal{L}_{ij} - \frac{1}{3}\mathcal{L}_{kk}\delta_{ij})\mathcal{M}_{ij} >}{< \mathcal{M}_{ij}\mathcal{M}_{ij} >} \tag{15}$$

where

$$\mathcal{L}_{ij} = \widehat{\overline{\rho}\tilde{u}_i\tilde{u}_j} - (\widehat{\overline{\rho}\tilde{u}_i})(\widehat{\overline{\rho}\tilde{u}_j})/\hat{\overline{\rho}} \tag{16}$$

and

$$\mathcal{M}_{ij} = -2\hat{\bar{\rho}}\hat{\Delta}^2|\hat{\tilde{S}}|(\hat{\tilde{S}}_{ij} - \frac{1}{3}\hat{\tilde{S}}_{kk}\delta_{ij}) + 2\Delta^2(\widehat{\bar{\rho}|\tilde{S}|\tilde{S}_{ij}} - \frac{1}{3}\widehat{\bar{\rho}|\tilde{S}|\tilde{S}_{kk}}\delta_{ij}) \quad (17)$$

The turbulent Prandtl number Pr_t is given by

$$Pr_t = \frac{C < \hat{\Delta}^2\hat{\bar{\rho}}\hat{\tilde{T}}_{,i}\tilde{T}_{,i} - \Delta^2\widehat{\bar{\rho}|\tilde{S}|\tilde{T}_{,i}\tilde{T}_{,i}} >}{< (\widehat{rho\tilde{u}_i}\,\widehat{\bar{\rho}\tilde{T}}/\hat{\bar{\rho}} - \widehat{\bar{\rho}\tilde{u}_i\tilde{T}})\tilde{T}_{,i} >} \quad (18)$$

where C is given by (15), and $<>$ indicates a volume averaging procedure which is needed to make the determination of C_I and the other SGS coefficients well conditioned. For all of the computations presented here, the ratio of the test-filter width to the grid-filter width $\hat{\Delta}/\Delta$ is taken as 2.0 and $C_I = 0.0$.

4 Numerical Method

The solutions to the Favre-averaged equations (1)-(4) are obtained numerically using implicit time integration with an approximately-factorized finite difference scheme. In the case of time accurate computations, the Newton-like sub-iteration scheme is employed. For the purpose of analysis, the Navier-Stokes equations are first cast into a general form:

$$U_{,t} + F(U) = 0 \quad (19)$$

where U is the vector of flow variables and $F(U)$ represents the nonlinear and viscous terms. An implicit approximation in time for this general equation can be written as [10]

$$[I + \frac{\vartheta\Delta t}{1+\varphi}\mathcal{A}(U^n)]\Delta U^n = -\frac{\Delta t}{1+\varphi}F(U^n) + \frac{\varphi}{1+\varphi}\Delta U^{n-1} \quad (20)$$

where $\mathcal{A} = F(U)_{,U}$ is the Jacobian of F. This equation is kept in what is called "Delta Form", referring to the $\Delta U^n = U^{n+1} - U^n$ term on the left hand side and is second order accurate in time for $\vartheta = \frac{1}{2}$,$\varphi = 0$ or $\vartheta = 1$,$\varphi = \frac{1}{2}$. It forms the basis for most implicit time integration schemes.

To represent the complex geometry using a body-fitted mesh and clustering points in the regions of high spatial gradient such as the boundary layer, a global, two-dimensional mapping is constructed from physical space (x, y, z) to a uniform, Cartesian computational space (ξ, η, z). Both ξ and η are in the range [0,1]. In computational space (ξ,η,z),the Jacobian $\mathcal{A}(U)$ can be written as [11]

$$\begin{aligned}\mathcal{A}(U) = {} & AU_{,\xi} + BU_{,\eta} + CU_{,z} + DU \\ & -V_{\xi\xi}U_{,\xi\xi} - V_{\xi\eta}U_{,\xi\eta} - V_{\xi z}U_{,\xi z} \\ & -V_{\eta\eta}U_{,\eta\eta} - V_{\eta z}U_{,\eta z} - V_{zz}U_{,zz}\end{aligned} \quad (21)$$

where $U = \{\rho, u, v, w, T\}^T$ is an unsteady flow field and the matrices (A, B, C, D, V_{ij}) are function of U and its gradients and also contain the metrics terms.

Substituting (21) into (20), and using conventional finite difference or finite volume schemes for the spatial derivatives usually results in large sparse matrix systems, which are not too difficult, but prohibitively time consuming, to solve directly. Approximate factorizations are employed to improve the efficiency, reduce the computer storage requirements and enhance numerical stability. Thus, factorized in the ξ, η, z directions, equation (20) can be written as:

$$[I + \alpha\Delta t(A\Delta_\xi + D - V_{\xi\xi}\Delta_{\xi\xi})]\mathcal{P} = \mathcal{R} \quad (22)$$

$$[I + \alpha\Delta t(B\Delta_\eta - V_{\eta\eta}\Delta_{\eta\eta})]\mathcal{Q} = \mathcal{P} \quad (23)$$

$$[I + \alpha\Delta t(C\Delta_z - V_{zz}\Delta_{zz})]\Delta U^n = \mathcal{Q} \quad (24)$$

where

$$\alpha = \frac{\vartheta}{1+\varphi},\ \mathcal{R} = -\frac{\Delta t}{1+\varphi}F(U^n) + \frac{\varphi}{1+\varphi}\Delta U^{n-1} \tag{25}$$

The factorizations introduce a $\mathcal{O}(\Delta t^2)$ error compared to the unfactorized equations. This factorization error can be eliminated by employing a subiteration time stepping procedure to recover the solution of (20). For this purpose, rewrite equation (20) by substituting a new iterative index $p+1$ for the $n+1$ terms and adding U^p to both sides of the equation, to obtain

$$[I + \frac{\vartheta\Delta t}{1+\varphi}\mathcal{A}(U^p)]\Delta U^p = -\frac{\Delta t}{1+\varphi}F(U^p) + (U^p - \frac{1+2\varphi}{1+\varphi}U^n + \frac{\varphi}{1+\varphi}U^{n-1}) \tag{26}$$

with $\Delta U^p = (U^{p+1} - U^p)$ and $\mathcal{A}(U^p) = \partial F/\partial U_p$. Equation (26) is the basic sub-iteration time advancement scheme which will yield second order time accuracy independent of choice of $\mathcal{A}(U^p)$ if the sub-iteration process converges. The n and $n-1$ terms are evaluated from previous time level and after iterating p times the solution at time level $n+1$ will be taken from the most recent U^{p+1}. For example, choosing $\varphi = \frac{1}{2}$ and $\vartheta = 1$, in the limit (assuming the iterative process converges) $U^{p+1} = U^p$, setting $U^{n+1} = U^{p+1}$, we have

$$\frac{3U^{n+1} - 4U^n + U^{n-1}}{2\Delta t} + F(U^{n+1}) = 0 \tag{27}$$

which is a second order in time, fully implicit approximation of equation (19).

This sub-iteration scheme requires that first the iterative process converge, and second the local sub-iteration process be performed until the error is of higher order in time. In practice one finds that two to three sub-iteration gives adequate accuracy for most problems.

For the spatial discretization, consider derivative operators in the uniform computational space (ξ, η) where ξ_i, η_i represent the nodal locations with $\xi_i = \Delta\xi(i-1)$ for $1 \le i \le N_\xi$ and $\eta_j = \Delta\eta(j-1)$ for $1 \le j \le N_\eta$. At interior nodes, the fourth-order-accurate central difference scheme is used for first and second derivatives.

$$\left(\frac{\partial f}{\partial \xi}\right)_i = \frac{1}{12\Delta\xi}[(f_{i-2)} - f_{i+2}) - 8(f_{i-1} - f_{i+1})] \tag{28}$$

$$\left(\frac{\partial^2 f}{\partial \xi^2}\right)_i = \frac{1}{12(\Delta\xi)^2}[-(f_{i-2} - 2f_i + f_{i+2} + 16(f_{i-1} - 2f_i + f_{i+1})] \tag{29}$$

Near the computational boundaries, finite difference operators that are biased toward the interior are required. As for the interior points, a five point stencil is used at the boundary grid point ξ_1. The resulting difference schemes are forth and third order accurate for the first and second derivatives respectively. Hence, At the first grid point ξ_1, the first and second derivative are expressed as :

$$\left(\frac{\partial f}{\partial \xi}\right)_1 = \frac{1}{12\Delta\xi}[-25f_1 + 48f_2 - 36f_3 + 16f_4 - 3f_5] \tag{30}$$

$$\left(\frac{\partial^2 f}{\partial \xi^2}\right)_1 = \frac{1}{12(\Delta\xi)^2}[11f_1 - 20f_2 + 6f_3 + 4f_4 - f_5] \tag{31}$$

while at the second point ξ_2, they are

$$\left(\frac{\partial f}{\partial \xi}\right)_2 = \frac{1}{12\Delta\xi}[-3f_1 - 10f_2 + 18f_3 - 6f_4 + f_5] \tag{32}$$

$$\left(\frac{\partial^2 f}{\partial \xi^2}\right)_2 = \frac{1}{12(\Delta\xi)^2}[35f_1 - 104f_2 + 11f_3 - 56f_4 + 11f_5] \tag{33}$$

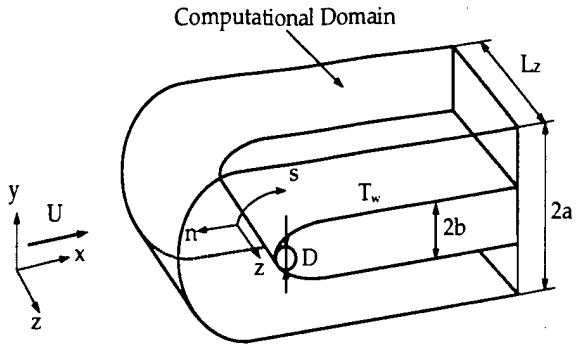

Figure 1: Flow configuration schematic

Similar expressions hold for the derivatives at nodes of $N_\xi - 1$ and N_ξ but with the stencils reversed and the signs switched on the coefficients for the first derivatives.

For the test filter in the dynamic SGS model, the following Simpson's rule is used:

$$\tilde{f}_i = \frac{1}{6}(f_{i-1} + 4f_i + f_{i+1}) \tag{34}$$

It is only applied in the homogeneous direction, where the grid is uniform so that the filtering and differential operation commute.

5 Initial and Boundary Conditions

The geometry and flow configuration are based on the experiments previously studied by Van Fossen *et al.*[5] and is shown in Fig. 1. A finite-thickness flat plate is placed horizontally in the center of the test section of a wind tunnel. The flat plate has an elliptical leading edge with a major to minor axis ratio 3:1 and is held at a uniform temperature. The flow is confined on four sides by walls which define the test section. The computational domain is $15D$,$10D$ and $1D$ in length, height and width. The inflow boundary is placed at $4D$ upstream of the leading edge and the isotropic homogeneous free-stream turbulence is convected into the domain from the inflow boundary and impinges on the leading-edge.

The boundary conditions used are as follows. On the body surface, no-slip and isothermal conditions are applied. The density is obtained from the continuity equation. At the outflow, the parabolized Navier-Stokes equation is solved using a known pressure gradient taken from previously computed potential flow solution[11]. On the inflow, the boundary conditions are based on the locally one-dimensional Riemann invariants. For a subsonic flow, four quantities must be specified. Here we constrain the entropy, spanwise and tangential velocity, and the incoming Riemann invariant. The locally one-dimensional Riemann invariants are defined in the direction normal to the inflow boundary as

$$R_1 = v_n - \frac{2c}{\gamma - 1}, \quad R_2 = v_n + \frac{2c}{\gamma - 1} \tag{35}$$

where c is the local speed of sound and v_n is the velocity normal to the boundary. Then on the inflow boundary,

$$\begin{aligned} s = s_\infty,\ w = w',\ v_t = \overline{v_t} + v_t', \\ R_1 = \overline{R}_1 + R_1', \quad R_2 = R_{2int} \end{aligned} \tag{36}$$

here the overline quantities denote the base flow in the absence of inflow turbulence, primed quantities represent the free-stream turbulence, and the subscript t denotes the tangential velocity along the inflow boundary in the $x - y$ plane. In the present computation, the inflow is not far away from the body and the flow passage is significantly blocked by the presence of the flat plate, so the potential solution should not be used directly to form the incoming Riemann invariant due to the development of the boundary layer on

the body. Hence we first compute the two dimensional steady base flow using the same set of the inflow conditions but in the absence of turbulence. The velocities $\overline{v}_t$ and $\overline{v}_n$ are determined by

$$\overline{\omega} = 0, \quad \overline{v}_n = v_{np} \tag{37}$$

Here ω is the vorticity at the inflow and v_{np} denote the normal velocity obtained from the potential solution. These overline quantities are used to form the $\overline{R}_1$ and the primed quantities are interpolated from the precomputed isotropic homogeneous turbulence. The interpolation is implemented using fourth order B-spline. The R_{2int} are computed from first order extrapolation from the interior domain $R_{2int} = 2R_{2N-1} - R_{2N-2}$. When the Riemann invariants are obtained, the values of v_n and c at the inflow can be obtained. When passing the free stream disturbance, the turbulence is multiplied by a function $exp(-(x/\Gamma)^2)$ so that turbulence only enters the center vertical portion near $x = 0$ of the inflow plane. This is reasonable since the turbulence far from the body in the transverse direction is not expected to impact the flow near the body.

6 Generation of Free-Stream Turbulence

In the present study, the mean flow at the inlet boundary is nearly uniform and shear-free, so the free-stream turbulence can not be generated within the computational domain. To have realistic free-stream turbulence, we performed a large eddy simulation of isotropic homogeneous turbulence separately. After the turbulent flow evolves from its initial field to a state with specified intensity and length scale, we use that flow field as the free stream turbulence and convect it into the domain using the boundary conditions (36).

Since the isotropic homogeneous turbulence is pre-computed in a finite domain, when it is passed as free-stream turbulence through the inflow, after a certain time the signal will repeat itself. To break this periodicity, phase jittering can be applied to the free stream turbulence data. However, to minimize the periodicity of the signal, and produce more realistic turbulence for the present flow configuration, we choose the computational domain to be a rectangular box which is $4D$, $4D$ and $1D$ in x, y and z direction. Accordingly, the grid size is 128x128x32 so that $\Delta x = \Delta y = \Delta z$, a necessary condition to preserve the isotropy of the turbulence. The numerical code for the large eddy simulation is adapted from an existing DNS code [12] by incorporating the same dynamic SGS model. The temporal and spatial discretization are fourth order Runge-Kutta and the sixth order compact finite difference scheme [13]. Periodic boundary conditions are applied in all spatial directions. The initial condition is a purely solenoidal velocity field with uniform density and temperature field. The initial three dimensional energy spectrum is of the form

$$E(k) \propto k^4 exp[-2(k/k_p)^2] \tag{38}$$

where the peak wavenumber of the spectrum k_p is taken as 8π. A few small wavenumbers which represent the long waves permissible in the x and y directions but not supported in z are zeroed out initially to preserve the turbulence isotropy. After the turbulence develops from its initial state, the isotropic turbulence field with intensity $u'_{rms}/u_\infty = 0.08$ and integral scale $L/D = 0.1$ is taken as our free-stream turbulence data. The turbulent Reynolds number at the inlet is $Re_L = u'_{rms}L/\nu = 80$.

7 Results

The computational grid in the x-y plane is generated by using an algebraic multi-surface method [14] which gives desirable orthogonality at the body surface and at the inflow/outflow boundaries. The grid is clustered towards the wall and the leading edge but is uniform in z since the flow is assumed homogeneous in the spanwise direction. Unlike the conventional C-type grid which is largely stretched toward the far upstream, the grid resolution at the inflow should be determined by the characteristic scale of the free-stream turbulence and in the present case should be as isotropic as possible. The grid used in the present simulation is of size 383x192x64 in the streamwise, normal and spanwise directions. The grid line distribution in $x - y$ plan is shown in Fig.2. The grid resolution at the inflow boundary is approximately the same as in the LES of isotropic homogeneous turbulence. To represent the experimental conditions accurately with the current flow configuration, the simulations are performed in a progressive way. We first generate the incompressible potential flow around the body with blockage effect taken into account, then use it as the initial condition to

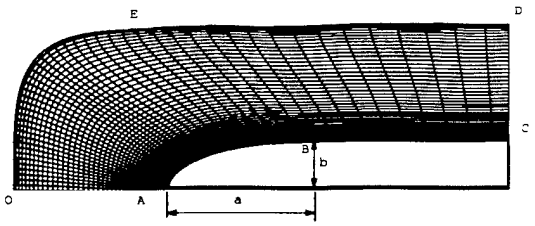

Figure 2: Computational mesh for the upper half of the domain in $x-y$ plane. For clarity, only every fourth grid line of a grid 384x192 grid is shown here.

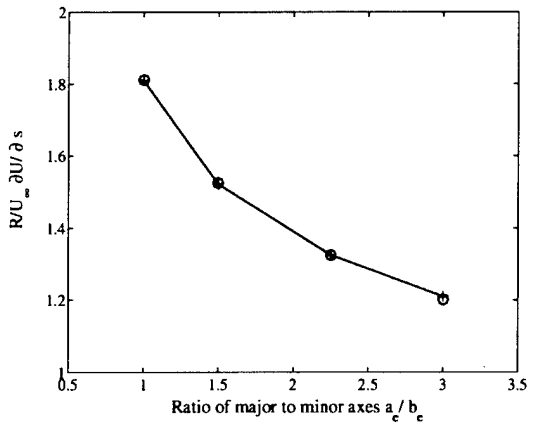

Figure 3: Leading edge velocity gradients. Solid line with plus sign is the present simulation, and the circles are taken from Van Fossen *et al* (1994).

compute the compressible potential flow. After the compressible potential solution is obtained , it serves as the initial condition and part of the boundary conditions for the two dimensional laminar viscous calculation. For the three dimensional case, we take the two dimensional viscous solution as the initial condition and performed the simulations with the inlet disturbances as i) laminar organized disturbances and ii) free-stream turbulence. The purpose of studying the steady organized disturbance is to gain insight into the basic interaction process at the leading edge and guide the choice of appropriate parameters for the free-stream turbulence case. In Van Fossen's experiments, four different models with the same leading edge diameter but different major to minor axes ratios from 1:1, 1.5:1, 2.25:1 to 3:1 were used to produce different leading edge velocity gradient. The same model parameters are used here for the two dimensional calculations. Fig. 3 shows the comparison of leading edge velocity gradients from the compressible potential solution $M = 0.2$ with the previous results obtained by a panel method[5]. Note the leading edge velocity gradients are affected significantly by the blockage effect, and the excellent agreement shows that this important feature of the experiments has been captured accurately.

The two dimensional viscous calculation is validated against analytical self-similarity solutions at the leading edge for heat conducting, compressible flow by Reshotko and Beckwith[15]. Fig. 4 and Fig. 5 show the comparisons between numerical and similarity solutions for the velocity and enthalpy profiles inside the boundary in the leading edge stagnation point region. Typically, the flow impinging on gas turbine blade is in the high subsonic or transonic regime, so the profiles shown here are for a high Mach number case $M = 0.8$. The low Mach number case $M = 0.2$, which corresponds to the experimental conditions, are also in excellent agreement with the similarity solutions. In these cases the ratio between wall temperature and free stream total temperature are 2.0 and Pr is taken as 1.0. As required to possess similarity solutions, the viscosity is assumed to be a linear function of temperature.

Before introducing the free stream turbulence at the inflow for large eddy simulation, the inflow boundary conditions based Riemann variants are tested. Fig. 6 show the contours of the disturbance velocities u, v and the vorticity ω when a circular Taylor vortex is entering domain. The velocity disturbance level

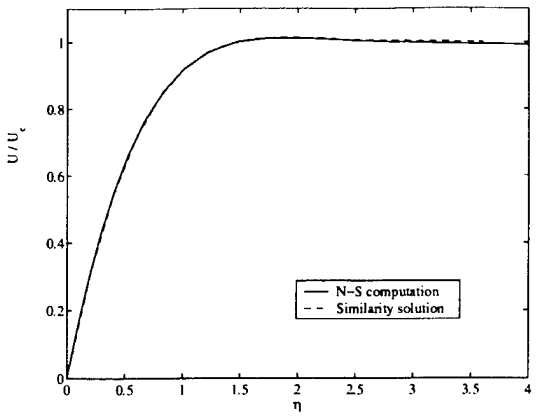

Figure 4: Comparison of boundary layer velocity profile at the leading edge. $Re = 10^5$, $M = 0.8$, $T_w/T_0 = 2.0$, $Pr = 1.0$.

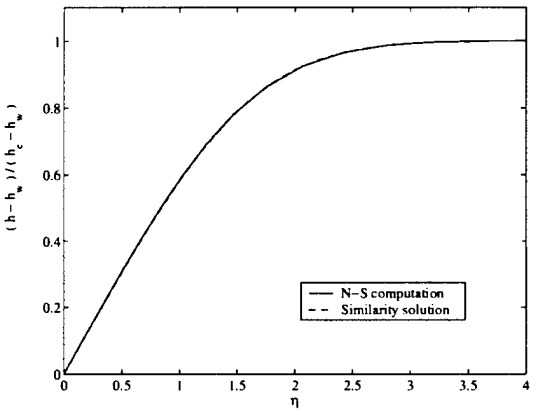

Figure 5: Comparison of boundary layer enthalpy profile at the leading edge. $Re = 10^5$, $M = 0.8$, T_w/T_0=2.0, $Pr = 1.0$.

$v_{max}/u_\infty = 15\%$ and radius of the vortex is $R_{Tayor}/D = 1.0$. It can be seen that vortex structures are kept fairly well even for this relatively large amplitude disturbance case.

The typical flow parameters for viscous laminar calculations are $Re_D = 20,000$, $M_\infty = 0.2$, $T_w/T_0 = 1.075$. where T_w and T_0 are the wall and total free stream temperature.The non-dimensional leading-edge heat transfer coefficient, or Frössling number, is defined as

$$Fr = \frac{Nu}{Re_D^{1/2}} = -\frac{T_{,n}}{\Delta T Re_D^{1/2}} \tag{39}$$

where the $T_{,n}$ is the nondimensional normal derivative of the temperature on the body surface. As in [7], the characteristic temperature difference ΔT for the evaluation of Fr is chosen to be the difference between the wall temperature and the adiabatic wall temperature $T_w - T_{aw}$. The adiabatic temperature can be approximated by

$$T_{aw} = \sqrt{Pr}\,(T_0 - T_{edge}) + T_{edge} \tag{40}$$

Here T_{edge} is the temperature at the edge of the boundary layer. Using the isentropic relation and assuming constant pressure across the boundary layer, the T_{edge} is obtained by

$$T_{edge} = T_t\,(\frac{P_{wall}}{P_0})^{(\gamma-1)/\gamma} \tag{41}$$

where P_0 is the free stream total pressure. For the two dimensional computation in the absence of inflow disturbances, Fr is obtained as $Fr = 0.748$. The corresponding experimental value for the 3:1 model gives $Fr = 0.750$ at a slightly higher Reynolds number.

For the organized disturbance case, a spanwise variation of the form $u = u_0(x,y) + \Delta u \sin(2\pi z/\Lambda)$ is imposed at the inflow for the streamwise velocity but the total temperature at the far upstream is kept constant. The wavelength is chosen to be in the range of 0.05D to 1.0D and the amplitude is $\Delta u = 0.05u_0$. Fig.7 shows the comparison of the heat flux distribution on the body surface with and without inflow disturbances. The value for the disturbed case is averaged over the spanwise direction. The heat transfer rate is increased by about 30% with 5% intensity of the incoming disturbances at $\Lambda = 0.1D$. The distribution of the heat transfer coefficient on the surface remains almost the same as for the undisturbed case, which is consistent with previous numerical and experimental studies. The dependence of heat transfer enhancement on the spanwise wavelength Λ is shown in Fig. 8. The enhancement decreases when the wavelength increases. But for very short wavelength, the disturbances are dissipated by viscosity and the flow reverts back to the two dimensional case. So an optimum wave length Λ_{opt} which gives maximum heat transfer enhancement is found around 0.1D for the present flow condition. Note that even though the stagnation point has the maximum heat transfer rate, the maximum increase in the local Fr occurs downstream of the stagnation point. When large heat transfer enhancement occurs, strongly 3D mushroom-like flow structure are observed due to the vortex stretching and the large reversed streamwise velocity at the leading edge. The typical temperature contour projected onto the stagnation plane corresponding to the high heat transfer rate is shown in Fig. 9.

Before we perform the LES of isotropic homogeneous turbulence in a rectangular box, the implementation of dynamic SGS stress model with compact difference scheme and Simpons 3-point filter are first validated through comparison with the DNS [16] and LES of the Comte-Bellot and Corrsin's experiments [17] in a cubic box. Excellent results have been obtained which validate the numerical scheme. These are not shown here for brevity. When applying to the current simulation in a rectangular box, initially the turbulence Reynolds number is set as $Re_L = 100$ with specified spectrum and random phase in spectral space. After small scale eddies develop and the turbulence become realistic, we stop the simulation at $Re_L = 80$ and save the data for later use as free stream turbulence. Turbulence integral scale L is determined by a least-squares curve-fitting to the autocorrelation data using an exponential function [5]

$$R(r) = e^{-r/L} \tag{42}$$

Data between $0.33 \le R(r) \le 1.0$ were used for curve fit. The exponential function does not have the correct limiting behavior for very small values of r, but the fit is satisfactory over the main domain and the fitted $R(r)$ can be integrated from 0 to ∞ to give the turbulence integral length scale. Fig. 10 shows the initial

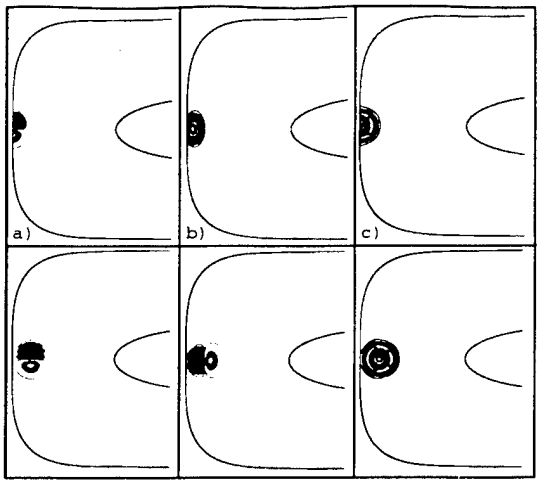

Figure 6: Passing a Taylor vortex through the inflow, upper row t=1.18, lower row t=2.35. a) streamwise velocity, b) transverse velocity, c) spanwise vorticity.

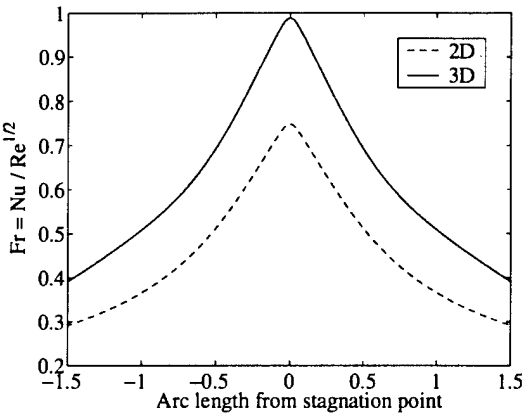

Figure 7: Heat transfer rate on the surface 2D laminar flow vs. spanwise averaged 3D case.

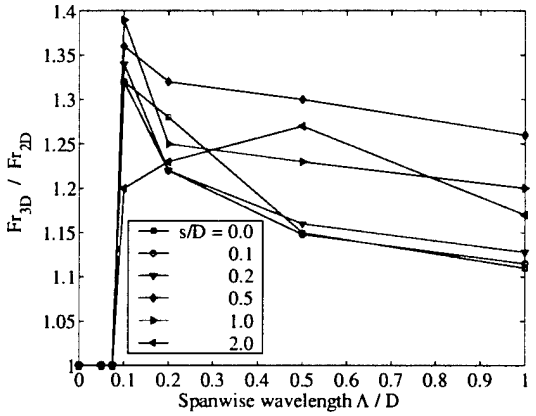

Figure 8: Increase of heat transfer vs spanwise wavelength at different streamwise locations on the body surface.

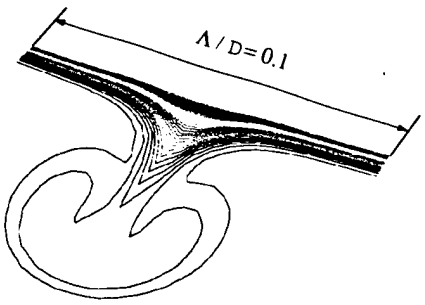

Figure 9: Temperature contours projected on the stagnation x-z plane.

and final three dimensional energy spectrum. Fig. 11 shows the velocity skewness reaches the typical value $-0.4\ -0.5$ for the realistic turbulence at Re_L about 80. The time development of turbulence kinetic energy is shown in Fig. 12. Notice that w'^2 is slightly larger than u'^2 and v'^2 in the time series, which may be caused by the different size of the computational domain in the z direction compared to the x and y directions. Since this lack of isotropy is small, it is not expected to have any major effect. As we started with the uniform density field, Fig. 13 shows the time development of the RMS value of density fluctuation. The time development of the dynamic model coefficient C is shown in Fig. 14.

Fig. 15 shows the turbulence intensity along the the stagnation stream line. The root-mean-square values are obtained by averaging u', v' and w' in time and in the spanwise direction. The turbulence is largely decaying until it reaches a distance of about D from the leading edge where the behavior of u', v' and w' changes. Notice that close to the body u' and w' are amplified while v' continues to decay. In Van Fossen's experiment, a power law curve of the form $Tu \sim x^m$ was used to fit the decay of free-stream turbulence in the absence of the model versus the distance downstream of the turbulence-generating grid. The power-law-fitted curve is also plotted in Fig. 15 with the same exponent $m = -0.83$ as used in the experiments. The fairly good agreement indicates that the initial decay rate of the free-stream turbulence has been captured correctly by the present simulation.

Fig. 16 uses a logarithmic scale on a slightly shifted x-axis to show the same data as in Fig. 15 with the leading edge region amplified for clarity. The transformation of the x-axis used here is $log(4.02 - x)$. Note $x = 4$ corresponds to the location of the leading edge. It reveals that the free-stream turbulence will go through three different processes as it impinges on the leading edge. First is the free turbulence decay process, corresponding to the distance from the inflow to approximately $x = 3$, when the presence of the body does not affect the turbulence significantly. The second process is the inviscid distortion process, approximately corresponding to the distance from $x = 3$ to $x = 3.95$, where the free-stream turbulence undergoes large mean flow strain caused by the diverging mean streamlines. A direct, quantitative comparison between the present results and the compressible rapid distortion theory (RDT)[18] is not easily obtained due to the viscous effect and the relatively small scale of turbulence, but the increase of u'_{rms} and w'_{rms}, and decrease of v'_{rms} are qualitatively in agreement with the temporal prediction of RDT under plane strain[19]. The third is the viscous interaction, which occurs within the leading edge boundary layer thickness. Also notable is that the spanwise velocity w'_{rms} continues to increase significantly while u'_{rms} and v'_{rms} start decreasing due to the presence of the wall. This is due to wall-blocking or splatting effect[20] [21].

Fig. 17 shows the vorticity components along the stagnation streamline. Clearly the transverse vorticity ω_y increases dramatically as the leading edge is approached. After being wrapped along the surface as the flow impinges on the leading edge, it forms large streamwise vorticity and produces the 'mushroom-like' flow structures downstream of stagnation point as clearly shown in Fig. 21, which are directly responsible for the heat transfer enhancement. Fig. 18 shows the time history of w_{rms} with the average taken only in the spanwise direction. At the inflow region, the presence of small scale turbulence is evident in the fluctuations of the signal. By the time the flow reaches the leading edge region, most of the small scales of turbulence are damped by the viscosity. However, under the strong strain imposed by the mean flow, the free-steam turbulence is re-organized into persistent flow structures, which significantly influence the boundary layer at the leading edge.

Fig.19 shows the spanwise correlation length L_c for u' along the stagnation streamline. Here L_c is defined

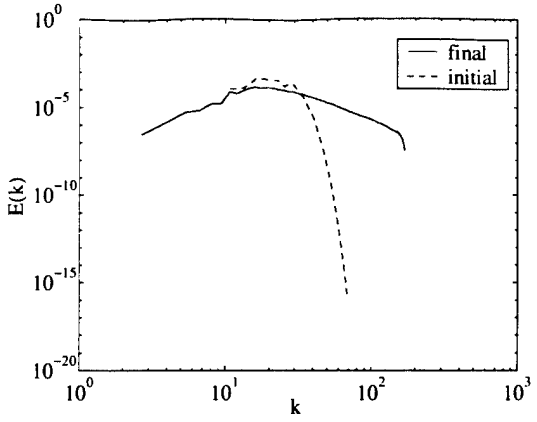

Figure 10: Initial and final three dimensional energy spectrum for isotropic homogeneous turbulence in a rectangular box.

as one half of the length at which the spanwise autocorrelation curve for u' first crosses zero. L_c can be regarded as a length scale characterizing the size of the energetic eddies in the spanwise direction. A very rapid decrease of L_c occurs in the leading edge region, indicating the strong vortex stretching effect. L_c reaches its minimum value at the outer edge of the boundary layer and then increases inside the boundary layer where viscosity is predominant. The minimum value of L_c is only about one third of its value at inlet. The ratio of the minimum L_c to the local boundary layer thickness δ is about 2-3. These observations suggest that the characteristic turbulence scale at the leading edge is largely determined by the local strain rate rather than by the free-stream turbulence scale at the inlet. Computationally, this will determine the required spanwise grid resolution in the leading edge region, because even with large eddy simulation, the grid has to be fine enough to resolve these "large eddies", especially in high Reynolds number case where the ratio of the turbulence length scales in the free-stream and at the leading edge is expected to increase.

The comparison of the Frössling number on the surface with and without free-stream turbulence is shown in Fig. 20. For the turbulent case, Fr is averaged over time and along the spanwise direction. The increase in Fr is about 11 %, and its distribution is very much the same as in laminar case. For the same flow configuration, the experiments [5] were carried out at a higher Reynolds number. If we extrapolate Frössling number increase over the laminar flow case using a correlation developed from high Reynolds number experimental data[5] to the conditions of the current simulations, a value of 10% is obtained. This extrapolation includes the effect associated with the decay of free-stream turbulence from the inlet to a location just outside the boundary layer[‡], as also done in reducing the experimental data.

The current computational value is in good agreement with the experimental correlation. The heat-transfer increase is, however, modest. This is because of the modest Reynolds number of the present LES. As discussed earlier the spanwise length scale decreases sharply within the boundary layer, and a new computation with refined resolution is currently underway. Fig. 22 shows an instantaneous heat flux contour on the blade surface. Clearly, the disturbances are largely stretched in the streamwise direction, and the strong streamwise vortices produce streak-like regions with high heat transfer rate.

8 Summary

The leading edge heat transfer enhancement under incoming organized disturbance and free-stream turbulence are investigated numerically. For the laminar organized disturbances, the three dimensional compressible Navier-Stokes equations are solved using high-order finite differencing and an implicit time marching scheme. Significant heat transfer increase is obtained for small inflow disturbance amplitude. The enhancement decreases with increased length scale, and an optimum length scale is found which gives maximum heat

[‡]In a conference paper AIAA-2001-1016, we had missed to account for this change, and incorrectly deduced that the heat-transfer augmentation observed in LES was lower than the experimental correlation.

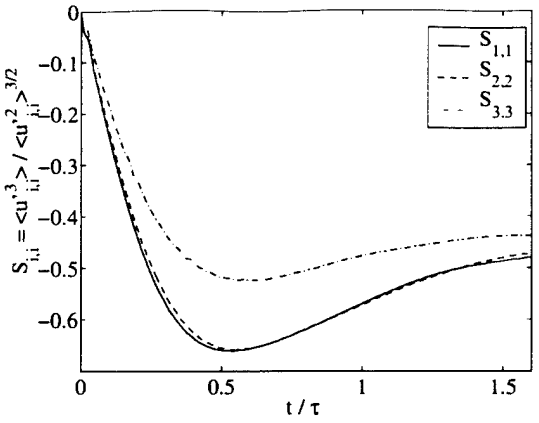

Figure 11: Time development of the velocity gradient skewness.$\tau = L/u_{rms}$, where L is the turbulence integral length scale.

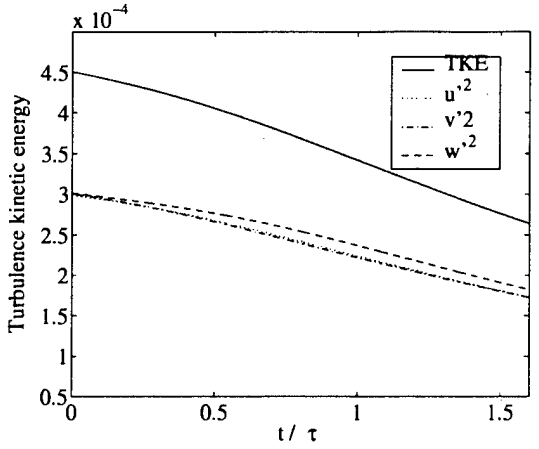

Figure 12: Time development of the turbulence kinetic energy.

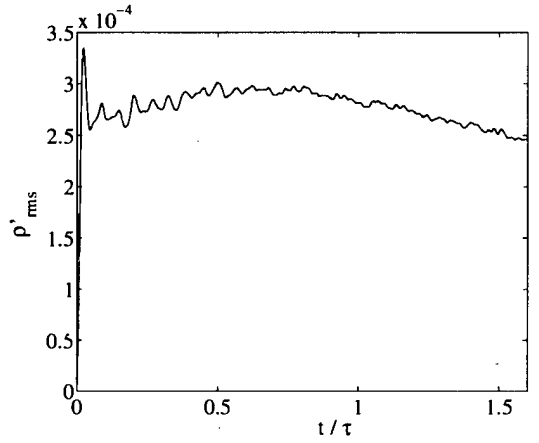

Figure 13: Time development of the density fluctuation.

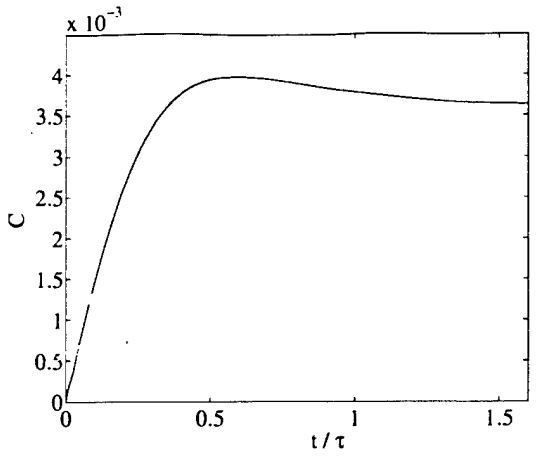

Figure 14: Time development of the dynamic SGS model coefficient C.

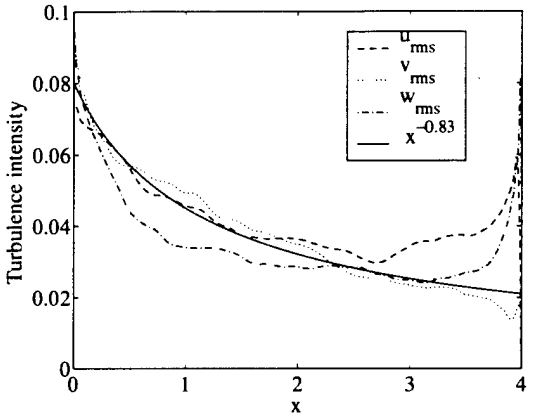

Figure 15: Turbulence intensity along the stagnation streamline. The solid line is a power law fit using the same the exponent (-0.83) as in Van Fossen's experiments.

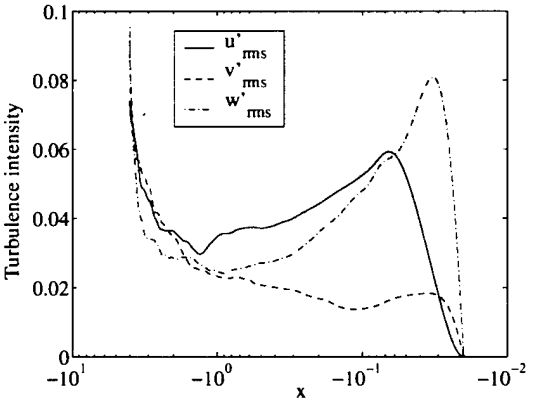

Figure 16: Turbulence intensity along the stagnation streamline, transformed x axis.

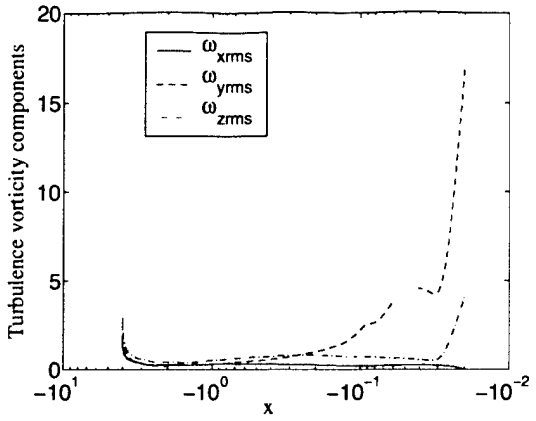

Figure 17: Turbulence vorticity components along the stagnation streamline, transformed x axis

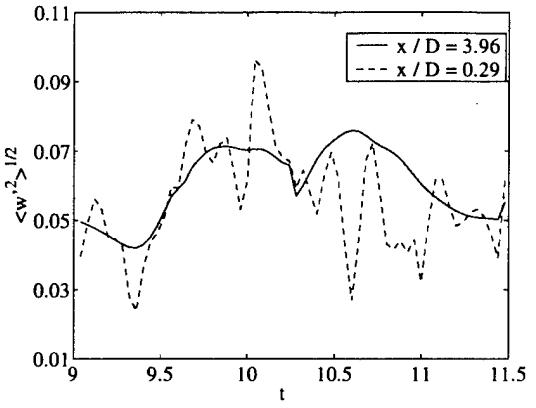

Figure 18: Time history of $< w'^2 >^{1/2}$ at locations close to inlet and leading edge along stagnation streamline. <> denotes the average in spanwise direction.

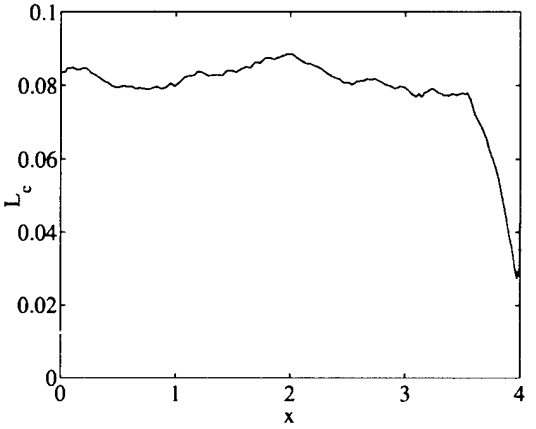

Figure 19: Spanwise correlation length for u' along the stagnation streamline.

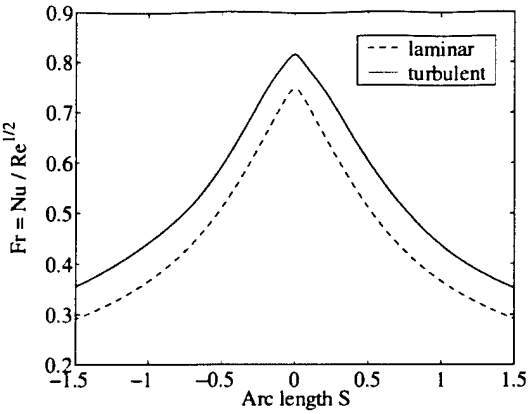

Figure 20: Frössling number distributions on the leading edge region.

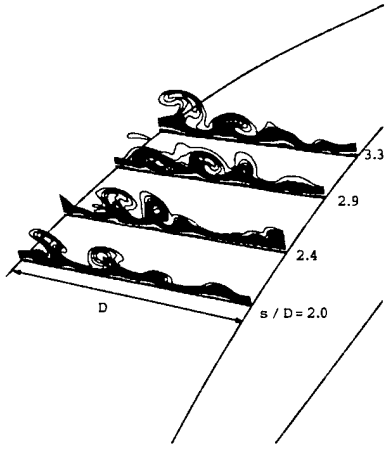

Figure 21: Cross section temperature contour at various streamwise locations.

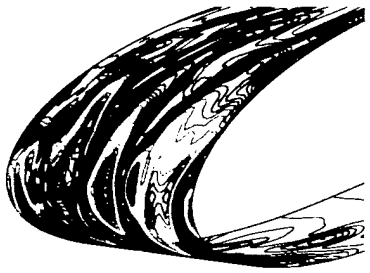

Figure 22: Heat flux contour on the leading edge with free-stream turbulence.

transfer increase. For the free-stream turbulence case, a large eddy simulation using the same algorithm with dynamic SGS model was performed. The free-stream turbulence used in the LES was generated by a separate large eddy simulation of homogeneous isotropic turbulence. The interaction of free-stream turbulence impinging on the leading edge was found to involve three distinct processes: free turbulence decay, inviscid distortion and viscous interaction. Strong streamwise vortices are formed on the wall through this interaction and are largely responsible for the heat transfer enhancement. The wall heat flux distribution under free-stream turbulence is found to keep almost the same shape as in the laminar case. Through the present simulation, it is observed that the typical energetic mushroom-like vortices which are formed at the leading edge are the direct cause of turbulent heat transfer enhancement. The size of these structures is typically 2-3 times the leading edge boundary layer thickness. To characterize the scale of these structures at different Reynolds number, as indicated in [8], the local boundary layer thickness would be a better choice than a fixed reference length such as D. This poses a severe challenge to a computational approach such as large eddy simulation, because it requires that these "large" energetic turbulence structures at the leading edge must be fully resolved to have an accurate prediction of turbulent heat transfer under free-stream turbulence. For the modest Reynolds number of the current simulations the predictions were found to agree well with experimental data. However, to capture the free-stream turbulence effects in higher Reynolds number flows it will be necessary to use a significantly refined grid within the boundary layer. Our results suggest that what is needed is, in effect, a hybrid simulation strategy where the turbulence outside and away from the blade surface is captured using LES techniques while a finer DNS-like grid is embedded within the near-wall region to resolve the smaller eddies responsible for near-wall effects. Such a methodology is being developed in an extension of the work supported under this grant.

One of the primary objectives of current research is to develop large eddy simulations as a tool for heat transfer prediction over a turbine blade immersed in a high-subsonic/transonic hot stream containing free stream turbulence. So the next logical step will be to extend the current simulation to a higher Mach number case, which is not easily investigated experimentally. The three dimensional moving wake caused by the upstream blade rows is another essential element of the flow impinging on a downstream blade row. Instead of isotropic homogeneous turbulence, wake turbulence can also be introduced as the free-stream disturbance. This combined study would provide a unique assessment of the important blade heat transfer mechanism relevant to the gas turbine environment.

9 Acknowledgments

This work is supported by the Air Force Office of Scientific Research under grant No. F94620-97-1-0047 with Dr. Tom Beutner as the program manager. The computer resource were provided by the Naval Oceanographic Office (NAVOCEANO) Major Shared Resource Center under DOD support. This grant has supported the Ph. D. thesis research of Zhongmin Xiong. It also provided partial support to the thesis research of Ted Manning (in its initial phase), who completed his Ph. D. in 1998. The work supported by the grant has been reported in the publication: Z. Xiong and S. K. Lele (2001) AIAA Paper 2001-1016 'Numerical study of leading edge heat transfer under free-stream turbulence', presented at the 39th AIAA Aerospace Sciences Meeting in Reno held during 8-11 January 2001.

References

[1] Kestin, J., (1966) The effect of free-stream turbulence on heat transfer rate. Adv. heat Transfer, 3, pp. 1-32.

[2] Kestin, J., Wood, R. T., (1970) The influence of turbulence on mass transfer from cylinders. ASME J. Heat Transfer, 92, pp. 321-327.

[3] Yeh, F.C., Hippensteels, S.A., Van Fossen, G.J., Poinsatte, P.E., and Ameri,A., (1993) High Reynolds number and turbulence effects on aerodynamics and heat transfer in a turbine cascade. AIAA paper, No.93-225.

[4] Ames, F. E., Moffat, R. J., (1990), Heat transfer with hight intensity large scale turbulence: the flat plate turbulent boundary layer and the cylindrical stagnation point. Report No. HMT-43, Thermosciences Division of Mechanical Engineering, Stanford University, Stanford, CA

[5] Van Fossen, G.J., Simoneau, R.J. and Ching, C.Y.(1995) Influence of turbulence parameters, Reynolds number and body shape on stagnation region heat transfer, J. Heat Transfer, Vol.117, pp 593-603.444.

[6] Sutera, S.P., (1965) Vorticity amplification in stagnation-point flow and its effect on heat transfer. J. Fluid Mech., 21, pp. 513-534.

[7] Rigby, D.L., Von Fossen,G.J.(1992) Increased heat transfer to elliptical leading edges due to spanwise variations in the free-stream momentum: Numerical and Experimental Results. AIAA paper 92-3070.

[8] Bae, S., Lele, S. K., Sung, H. J.,(2000) Influence of inflow disturbances on stagnation-region heat transfer. ASME J. Heat Transfer, Vol. 122, pp. 258-265.

[9] Moin, P., Squires, K., Cabot, W., Lee, S.(1991) A dynamic subgrid-scale model from compressible turbulence and scalar transport. Phys. of Fluids A, Vol.3, pp 2746-2757.

[10] Pulliam, T.H., (1993) Time accuracy and the use of implicit methods.AIAA Paper 93-3360.

[11] Collis, S.S., Lele, S.K. (1999) Receptivity to surface roughness near a swept leading edge, J. Fluid. Mech. Vol. 380, pp 141-168.

[12] Lui, C., Lele, S.K., (2001) Direct numerical simulation of spatially developing compressible turbulent mixing layers. AIAA paper 2001-0291.

[13] Lele, S. K., (1992) Compact finite difference schemes with spectral-like resolution. J. Comput. Phys. Vol. 103, 16-42.

[14] Eiseman, P. (1985), Grid generation for fluid mechanics. Ann. Rev. Fluid Mech, Vol. 17, pp. 487-522.

[15] Reshotko, E., Beckwith, I.E.(1958) Compressible laminar boundary layer over a yawed infinite cylinder with heat transfer and arbitrary Prandtl number. NACA Rep. 1379

[16] Lee, S., Lele, S. K., Moin, P., (1991), Eddy shocklets in decaying compressible turbulence. Phys. Fluids, A 3(4) pp. 657-664.

[17] Comte-Bellot, G., Corrsin, S. (1971) Simple eulerian time correlation of full and narrow-band velocity signals in grid generated 'isotropic' turbulence. J. Fluid Mech. Vol. 48, pp. 273-337.

[18] Goldstein, M.E., (1978) Unsteady vortical and entropic distortions of potential flows round arbitrary obstacles. J. Fluid Mech. Vol.89, pp. 433-468.

[19] Batchelor, G. K., Proudman, I. (1954) The effect of rapid distortion of a fluid in turbulent motion. Quart. J. Mech. Appl. Math. 1, 83.

[20] Hunt, J.C.R., Graham, J.M.R. (1978) Free-stream turbulence near plane boundaries. J. Fluid Mech. Vol. 84, pp. 209-235.

[21] Perot, B., Moin, P. (1995) Shear-free turbulent boundary layers. Part 1. Physical insights into near-wall turbulence. J. Fluid Mech. Vol. 295, pp. 199-227.